

Multidimensional quantum-beat spectroscopy: Towards the complete temporal and spatial resolution of the nuclear dynamics in small molecules

Martin Winter and Rüdiger Schmidt

Institut für Theoretische Physik, Technische Universität Dresden, D-01062 Dresden, Germany

Uwe Thumm

James R. Macdonald Laboratory, Kansas State University, Manhattan, Kansas 66506-2604, USA

(Received 13 March 2009; published 1 September 2009)

We propose a multidimensional (MD) pump-probe method to image the coupled rovibrational (RV) nuclear dynamics in small molecules. We apply this imaging method to analyze the laser-induced coherent RV nuclear dynamics in D_2^+ in terms of MD quantum-beat (QB) spectra, without and including an external laser field, by solving the time-dependent Schrödinger equation in full dimensionality. These spectra resolve the internuclear distance R and molecular orientation and reveal (1) the transition frequencies between stationary vibrational and rotational states, (2) their nodal structures, (3) RV couplings, including (4) their influence on the nuclear dynamics on field-free ground state and laser-dressed potential surfaces, and (5) offer an interpretation for an unexplained structure in recently measured QB spectra.

DOI: [10.1103/PhysRevA.80.031401](https://doi.org/10.1103/PhysRevA.80.031401)

PACS number(s): 42.50.Md, 33.20.Tp, 82.37.Np

Impressive advances in multi-time scale spectroscopic methods have transformed nuclear magnetic resonance spectroscopy into a powerful imaging technique, using the so-called “two-dimensional (2D) Fourier-transformation (FT) spectroscopy [1]” and have recently allowed for the identification of reaction pathways in complex biochemical reactions, e.g., in light-harvesting photosynthetic proteins [2] and in polypeptides during conformational changes [3]. In 2D FT spectroscopy, spatial and temporal resolutions are obtained by exciting a target with a sequence of three synchronized mutually delayed fs laser pulses and the delayed detection of the three-pulse photon echo in amplitude and phase. Subsequent FT with respect to two delay times yields 2D frequency maps of the target’s response from which information on the transient refraction, absorption, and structure of the target can be extracted. This novel method is capable of resolving the intramolecular and intermolecular flow of (vibrational and excitonic) energy in space and time with nanometer and femtosecond (fs) resolution [1,2].

In this Rapid Communication we present an alternative imaging method, multidimensional-quantum-beat (MD-QB) spectroscopy, that allows for the resolution of the nuclear dynamics in frequency and two spatial degrees of freedom. This method extends conventional (two pulse and one-dimensional) pump-probe spectroscopy that, in conjunction with advanced fs laser technology, is rapidly promoting the observation, analysis, and control of the nuclear dynamics in small molecules [4–9], thereby contributing significantly toward reaching the ultimate goals of imaging and steering complex chemical reactions with laser light [10–13]. For diatomic molecules, the MD-QB method directly provides temporal resolution [in terms of fragment-kinetic-energy-release (KER) spectra [4–6,14,15] taken for a sequence of pump-probe delays τ] and spatial information [obtained by “Coulomb explosion (CE)” imaging by the probe laser pulse from the KER [16,17]]. The CE imaging technique has been applied in pump-probe experiments to reveal not only the classical motion of the nuclear wave packets’ center of mass

but also purely quantum-mechanical effects, such as cycles of wave-packet dephasing and revival [4,6,8,14,18], in agreement with theoretical predictions [16]. By solving the time-dependent Schrödinger equation (TDSE) in full dimensionality for electrons and nuclei, we illustrate the MD-QB imaging method for the example of the simplest molecule, D_2^+ , and obtain complete information of the rovibrational

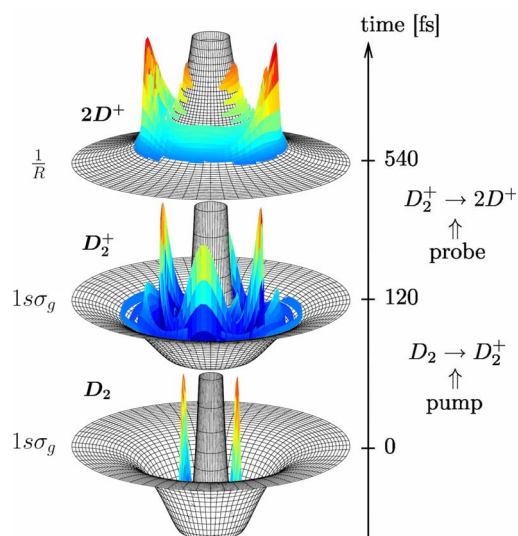


FIG. 1. (Color online) Snapshots of the calculated time evolution of a RV wave packet in $D_2^{0,+2+}$. At time $t=0$ a pump laser pulse ionizes D_2 and excites the initial RV wave packet (colored part) from the $1s\sigma_g$, $\nu=0$ state in D_2 (bottom graph) to the $1s\sigma_g$ state of D_2^+ where it evolves, continuously changing its distribution in R and θ . Middle graph: probability density of the wave packet in D_2^+ at $t=120$ fs. Ionization by a probe laser pulse after a delay of, e.g., $\tau=540$ fs projects the wave packet onto the repulsive ($1/R$) potential surface of the $2D^+$ -system (top graph), leading to fragmentation by CE. Measurement of the KER of the D^+ fragments as a function of τ enables the characterization of the wave-packet dynamics in terms of R - and θ -dependent spectra.

(RV) nuclear dynamics induced by a short and intense laser pulse (Fig. 1). In particular, we show that the second, rotational degree of freedom in D_2^+ determines the structure of QB spectra over a large frequency range *even* if only one spatial degree of freedom (R) is resolved, allowing a consistent interpretation of up to now unexplained experimental data [11].

Apart from quantum-classical hybrid models [19], by far most theoretical investigations of the laser-driven nuclear motion in diatomic molecules neglect molecular rotation and assume that the nuclei remain aligned along the linear polarization of pump and probe pulses [4,8,11,17,20]. While the rotation period T_{rot} of D_2^+ is more than an order of magnitude larger than the vibration period (≈ 22 fs), a comprehensive study of the nuclear motion needs to include the molecular orientation angle θ even for laser pulses that are short compared to T_{rot} in order to correctly account for the nuclear evolution for times $\geq T_{rot}$ [6,18,19,21–23].

We performed exact quantum-mechanical calculations for the coupled electronic and nuclear motion in D_2^+ in a linearly polarized laser electric field for times $T \gg T_{rot}$ and analyze the RV nuclear probability density in terms of R - and θ -dependent QB spectra. The energy resolution of these spectra can be systematically improved by increasing T , which we choose sufficiently large (49 ps) to resolve the beat frequencies between all occupied rotational and vibrational levels [20].

The QB imaging scheme consists in first eliminating the static background ρ_{stat} in the nuclear probability density ρ and then Fourier transforming $\rho_{dyn}(R, \theta, \tau) = \rho(R, \theta, \tau) - \rho_{stat}(R, \theta)$ as a function of τ over the *finite* delay interval $0 < \tau < T$ at fixed R and θ . This provides the R - and θ -dependent representation of the nuclear density $\tilde{\rho}_{dyn}(R, \theta, f)$ as a function of the frequency f . We define R - and θ -dependent power spectra $A(R, f) = |\int \sin(\theta) d\theta \tilde{\rho}_{dyn}(R, \theta, f)|^2$ and $W(\theta, f) = |\int dR \tilde{\rho}_{dyn}(R, \theta, f)|^2$ and the corresponding spectral line intensities $\mathcal{A}(f) = \int dR A(R, f)$ and $\mathcal{W}(f) = \int d\theta \sin(\theta) W(\theta, f)$.

In order to obtain $\rho(R, \theta, \tau) = \int d^3r |\psi(\vec{R}, \vec{r}, \tau)|^2$, we solve the time-dependent Schrödinger equation for D_2^+

$$i \frac{\partial}{\partial t} \psi(\vec{R}, \vec{r}, t) = \{\hat{T} + \hat{H}_{el}(\vec{r}; \vec{R}) + \epsilon(t)z\} \psi(\vec{R}, \vec{r}, t), \quad (1)$$

where \vec{r} denotes the electronic coordinate, \hat{T} the nuclear kinetic energy, and \hat{H}_{el} denotes the electronic Hamiltonian. We use atomic units throughout this Rapid Communication unless noted otherwise. The laser-electric field $\epsilon(t) = \epsilon_0 f(t) \cos \omega_L t$ is assumed to be linearly polarized along the z axes and is expressed in terms of the carrier frequency ω_L , amplitude ϵ_0 , and envelope $f(t)$. We expand the total wave function of D_2^+ in the external laser field in terms of field-free adiabatic electronic wave functions $\{\varphi_i\}$ with corresponding energy surfaces $\{E_i(R)\}$,

$$R \psi(\vec{R}, \vec{r}, t) = \sum_i \Omega_i(\vec{R}, t) \varphi_i(\vec{r}; \vec{R}), \quad (2)$$

and solve the electronic Schrödinger equation,

$$\hat{H}_{el}(\vec{r}; \vec{R}) \varphi_i(\vec{r}; \vec{R}) = E_i(R) \varphi_i(\vec{r}; \vec{R}), \quad (3)$$

for a large number of fixed internuclear distances [24].

Neglecting all non-Born-Oppenheimer (BO) dynamical couplings between the states $\{\varphi_i\}$ and inserting Eq. (2) into Eq. (1) leads to a set of coupled equations for the nuclear wave function $\vec{\Omega}(R, \theta, t) = (\Omega_1(R, \theta, t), \Omega_2(R, \theta, t), \dots)$,

$$i \frac{\partial}{\partial t} \vec{\Omega}(R, \theta, t) = [\hat{T} + \hat{E}(R) + \hat{D}(R, \theta, t)] \vec{\Omega}(R, \theta, t). \quad (4)$$

The matrix \hat{T} is diagonal with elements $-(1/2\mu)\partial^2/\partial R^2 + \hat{L}^2/2\mu R^2$. \hat{L} is the nuclear angular momentum, and μ is the reduced mass of the nuclei. \hat{E} has elements $E_{ij}(R) = E_i(R) \delta_{ij}$, and \hat{D} is the dipole coupling matrix with elements $D_{ij}(R) = \int d^3r \varphi_i^*(\vec{r}; \vec{R}) z \varphi_j(\vec{r}; \vec{R}) \epsilon(t)$. We propagate Eq. (4) numerically [25] and find converged results by including the three lowest BO potential surfaces of D_2^+ . We construct the initial wave function $\Omega_1(R, \theta, 0)$ as the product of a vibrational Franck-Condon wave function $\chi(R)$ on the ground-state BO potential surface of D_2^+ [20] and an angular wave function $\sum_{l=0,2,4} b_l P_l(\theta)$ given by the coherent sum of three even Legendre polynomials P_l with coefficients equal to the normalized square roots of a $T_B = 250$ K Boltzmann distribution, $b_l^2 = e^{-l(l+1)/2\mu R^2 k T_B} / \sum_{l'=0,2,4} e^{-l'(l'+1)/2\mu R^2 k T_B}$.

We first discuss the nuclear dynamics in D_2^+ *without* an external laser field. Initiated in the $1s\sigma_g$ surface of D_2^+ , the nuclear wave functions Ω_i remain uncoupled, and we only need to consider the $1s\sigma_g$ component

$$\Omega_1(R, \theta, t) = \sum_{v,l} a_{v,l} e^{-iE_{v,l} t} \chi_{v,l}(R) P_l(\theta), \quad (5)$$

which is expanded in terms of stationary vibrational states $\{\chi_{v,l}\}$ of D_2^+ with RV energies $\{E_{v,l}\}$. Using the orthogonality of $\chi_{v,l}$ and $\chi_{v',l'}$ and all $\{P_l\}$, the power spectra become

$$A(R, f) = \left| \sum_{v \neq v', l} a_{v,l} a_{v',l'}^* \chi_{v,l}(R) \chi_{v',l'}^*(R) \delta_T(f_{v,l,v',l'} - f) \right|^2, \quad (6)$$

$$W(\theta, f) = \left| \sum_{v,l \neq l'} a_{v,l} a_{v',l'}^* S_{v,l,v',l'} P_l(\theta) P_{l'}(\theta) \delta_T(f_{v,l,v',l'} - f) + \sum_{v \neq v', l \neq l'} a_{v,l} a_{v',l'}^* S_{v,l,v',l'} P_l(\theta) P_{l'}(\theta) \delta_T(f_{v,l,v',l'} - f) \right|^2, \quad (7)$$

where $\delta_T(f) = \int_0^T dt e^{-i2\pi f t}$, $2\pi f_{v,l,v',l'} = E_{v,l} - E_{v',l'}$, and $S_{v,l,v',l'} = \int_0^\infty dR \chi_{v,l}(R) \chi_{v',l'}^*(R)$. These spectra are peaked at the beat frequencies $f_{v,l,v',l'}$ where their dependence on R and θ expresses the nodal structure of (pairs of) vibrational and angular wave functions, respectively (Fig. 2).

Compared with the power spectra [Figs. 2(a) and 2(c)] and line intensities [Figs. 2(b) and 2(d)] for aligned molecules, rotation leads to the splitting of every $v \rightarrow v'$ vibrational beat frequency into multiple lines [Figs. 2(e)–2(h)] that correspond to different rotational states l in Eq. (6). This rotational substructure is recognized at high resolution in Figs. 2(g) and 2(h) as the splitting of the two lowest vibra-

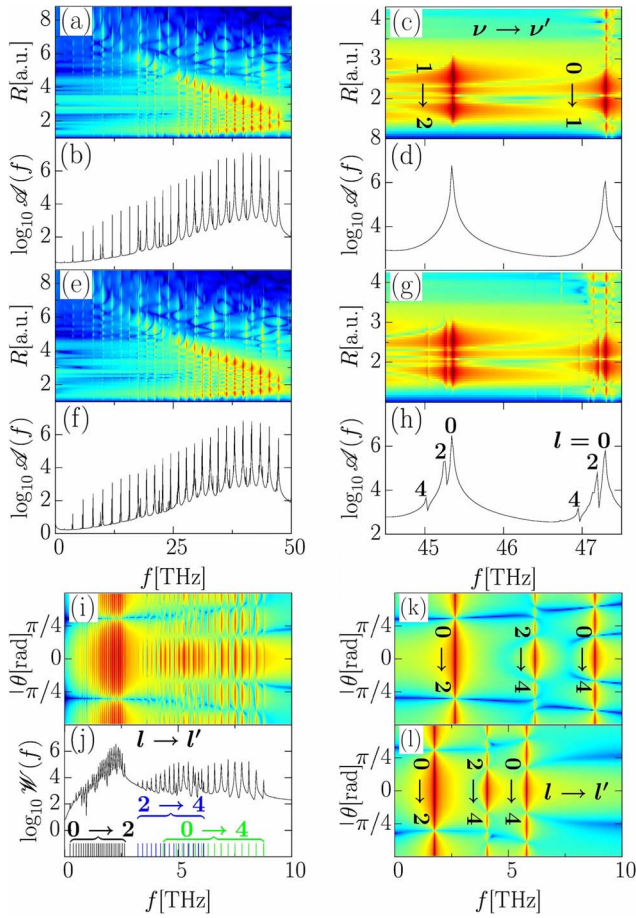


FIG. 2. (Color online) Power spectra $A(R, f)$, $W(\theta, f)$ and line intensities $\mathcal{A}(f)$, $\mathcal{W}(f)$ of the RV dynamics in D_2^+ without [(a)–(d)] and including molecular rotation [(e)–(l)]. [(a), (c), (e), and (g)] show $A(R, f)$; [(b), (d), (f), and (h)] corresponding $\mathcal{A}(f)$. (i): $W(\theta, f)$; (j): corresponding $\mathcal{W}(f)$. (k), (l): $W(\theta, f)$ in fixed rotor approximation, with an internuclear distance equal to the expectation value of R^{-2} in the $1s\sigma_g$, $\nu=0$ vibrational ground (k) and $\nu=10$ excited state (l).

tional beat frequencies into RV multiplets. The appearance of such multiplets of lines is due to *RV couplings*, i.e., to the fact that the energies $E_{\nu l}$ cannot be written as a sum of vibrational and rotational energies ($E_{\nu l} \neq E_\nu + E_l$). If this were possible, the RV manifolds would collapse to just one line at $2\pi f_{\nu l, \nu' l'} = (E_\nu + E_l) - (E_{\nu'} + E_{l'}) = E_\nu - E_{\nu'}$. To find out which vibrational transition belongs to which l , we add the rotational kinetic energy $l(l+1)/(2\mu R^2)$ to the ground-state BO surface to obtain $V_{\text{eff}}(R) = E_1(R) + l(l+1)/(2\mu R^2)$. In this effective potential the distances between the vibrational eigenenergies are smaller for larger l and the frequencies $f_{\nu l, \nu' l'}$ lower [Fig. 2(h)].

The field-free results in Figs. 2(a), 2(c), 2(e), and 2(g) display the nodal structure of the stationary vibrational states in the $1s\sigma_g$ of D_2^+ and thus retrace, near the classical turning points, the contour of the $1s\sigma_g$ BO potential curve (strictly speaking its derivative [20]). Similarly, the nodal structure of products of rotational eigenstates $P_l(\theta)$ is mapped onto the θ -dependent power spectra [Fig. 2(i)]. As shown in the dominant first term of Eq. (7), there is a series of rotational l

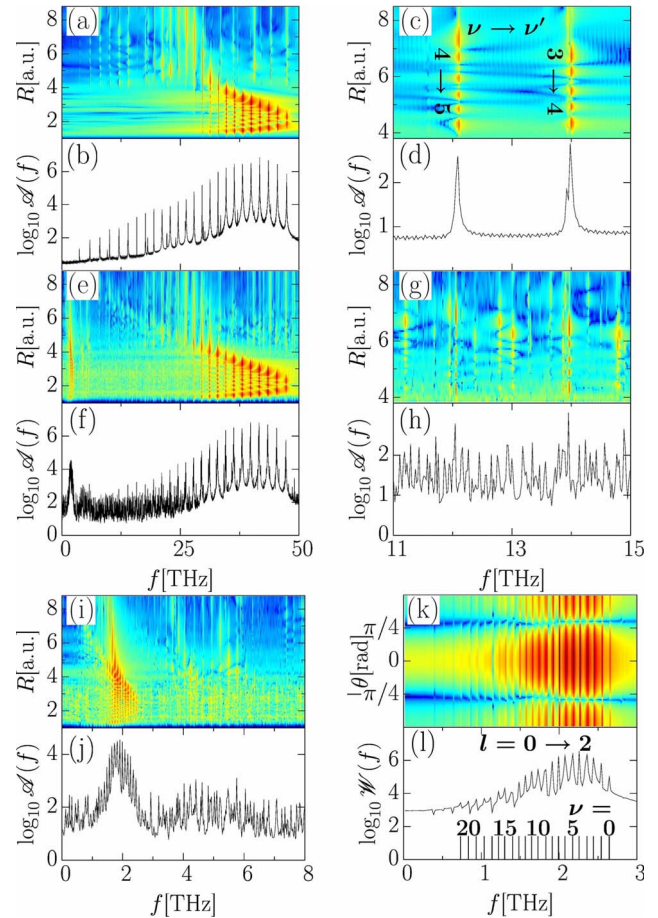


FIG. 3. (Color online) Power spectra $A(R, f)$, $W(\theta, f)$ and spectral line intensities $\mathcal{A}(f)$, $\mathcal{W}(f)$ of the RV wave-packet dynamics in D_2^+ under the influence of a probe pulse pedestal, without [(a)–(d)] and including [(e)–(l)] molecular rotation. [(c), (d) and (g), (h)] are frequency and radius zooms into the BH region of (a) and (e). [(i) and (j)] are frequency zooms of (e) and (f) into the rotation-dominated part of the spectrum. [(k) and (l)]: $W(\theta, f)$ and $\mathcal{W}(f)$ within the “bump”-shaped region in (i) and (j) around $f=2$ THz.

$\rightarrow l'$ transitions with a different nodal structure in θ for every vibrational state ν . For fixed l and l' , the $f_{\nu l, \nu' l'}$ decrease for increasing ν [Fig. 2(j)]. Note that all these lines would coincide in the absence of RV coupling.

The nodal structures in Fig. 2(i) can be easily understood in comparison with the rigid rotor approximation for D_2^+ [Figs. 2(k) and 2(l)] whose kinetic energy is the expectation value of the rotational energy, $\tilde{L}^2/(2m)\langle R^{-2} \rangle$ in $\chi_{\nu l}$ for a fixed vibrational quantum number ν . We chose $\nu=0$ [$\langle R^{-2} \rangle = 0.2455$, Fig. 2(k)] and $\nu=10$ [$\langle R^{-2} \rangle = 0.1615$, Fig. 2(l)], resulting in noticeably shifted rotational transitions lines. The lowest spectral lines in Figs. 2(k) and 2(l) are rotational QBs of the $l=0$ and $l=2$ rotational states (P_l has l nodes). The next spectral line has six nodes and corresponds to QBs of $l=2$ with $l=4$ states. The third spectral line, which is distinctly visible in both spectra, corresponds to the interference of $l=0$ and $l=4$ stationary states, whose energy difference for $\nu=0$ and 10 states is larger than for the other two lines. Note that the $l=2 \rightarrow 4$ line for $\nu=0$ has a higher energy than the $l=0 \rightarrow 4$ transition for $\nu=10$. Accordingly, series of rotational

beat frequencies for different Δl overlap [Figs. 2(i) and 2(j)].

Our results for the evolution of a RV wave packet under the influence of a 50 fs (full width-half maximum) 10^{13} W/cm² sin²-shaped probe pulse pedestal are shown in Fig. 3. This calculation reproduces all RV-coupling effects in the field-free scenario in Fig. 2. In addition, the R -dependent rotation-free power spectra in Figs. 3(a) and 3(e) show dissociation via “ $1-\omega$ bond softening.” Figure 3(a) shows weak evidence for transiently trapped “bond hardening (BH)” [20,26], which mostly disappears after the inclusion of molecular rotation in Fig. 3(e). As for the field-free case in Fig. 2, vibrational lines of the nonrotating molecular ion [Figs. 3(a)–3(d)] split into RV multiplets once the ion is allowed to rotate [Figs. 3(e)–3(l)]. The combined effect of laser-dressing and rotation diffuses the but distinct BH vibrational QB lines in Figs. 3(c) and 3(d) into spread out very faint multiplets in Figs. 3(g) and 3(h).

At lower frequencies, purely vibrational lines disappear for $R \lesssim 4$ [Fig. 3(a)], exposing lines that originate in RV couplings and occur at identical QB frequencies in Figs. 3(i) and 3(j) and Figs. 3(k) and 3(l) in R - and θ -dependent spectra, respectively. Note, in particular, that these lines do not occur in the field-free case [Fig. 2(e)] because in this case the RV-wave functions (5) factorize. Below 3 THz all lines in Figs. 3(k) and 3(l) are due to vibrationally split $l=0 \rightarrow 2$ QBs,

consistent with the two angular nodes in Fig. 3(k). Note further that exactly the same RV beat frequencies, which appear in the θ -dependent spectrum for all vibrational states [Fig. 3(l)], also occur in the R -dependent spectrum [Figs. 3(i) and 3(j)]. These RV couplings in the presence of the laser field match the up to now unexplained “rotational excitation” lines in the first measured R -dependent QB spectra [11].

In conclusion, we presented an application of MD-QB spectroscopy to analyze the coherent RV nuclear motion in D_2^+ . We discussed how this method reveals the nodal structure of bound RV states. In contrast to earlier studies for nonrotating molecules, our numerical propagation of RV wave packets generates QB spectra that display RV coupling effects and help in identifying such effects in recent proof-of-principle measurements [11]. For the future, MD-QB spectroscopy offers an approach for imaging laser-dressed potential surfaces and for quantifying both, RV coupling and field-dressed effects in molecules based on a time series of measured KER spectra.

We thank Burkhard Schmidt for helpful discussions. This work was supported by the NSF and the Division of Chemical Sciences, Office of Basic Energy Sciences, Office of Energy Research, and U.S. DOE.

-
- [1] D. M. Jonas, *Annu. Rev. Phys. Chem.* **54**, 425 (2003).
 [2] T. Brixner *et al.*, *Nature (London)* **434**, 625 (2005).
 [3] J. Bredenbeck *et al.*, *J. Phys. Chem. B* **107**, 8654 (2003).
 [4] A. S. Alnaser *et al.*, *Phys. Rev. A* **72**, 030702(R) (2005).
 [5] F. Légaré *et al.*, *Phys. Rev. A* **72**, 052717 (2005).
 [6] Th. Ergler *et al.*, *Phys. Rev. Lett.* **97**, 193001 (2006).
 [7] S. Baker *et al.*, *Science* **312**, 424 (2006).
 [8] D. S. Murphy *et al.*, *J. Phys. B* **40**, S359 (2007).
 [9] A. S. Sandhu *et al.*, *Science* **322**, 1081 (2008).
 [10] A. Staudte *et al.*, *Phys. Rev. Lett.* **98**, 073003 (2007).
 [11] B. Feuerstein *et al.*, *Phys. Rev. Lett.* **99**, 153002 (2007).
 [12] F. He, A. Becker, and U. Thumm, *Phys. Rev. Lett.* **101**, 213002 (2008).
 [13] F. Krausz and M. Ivanov, *Rev. Mod. Phys.* **81**, 163 (2009).
 [14] H. Niikura, D. M. Villeneuve, and P. B. Corkum, *Phys. Rev. A* **73**, 021402(R) (2006).
 [15] F. Martín *et al.*, *Science* **315**, 629 (2007).
 [16] B. Feuerstein and U. Thumm, *Phys. Rev. A* **67**, 043405 (2003); **67**, 063408 (2003).
 [17] S. Chelkowski, A. D. Bandrauk, A. Staudte, and P. B. Corkum, *Phys. Rev. A* **76**, 013405 (2007).
 [18] I. A. Bocharova *et al.*, *Phys. Rev. A* **77**, 053407 (2008).
 [19] M. Uhlmann, T. Kunert, and R. Schmidt, *Phys. Rev. A* **72**, 045402 (2005) and references therein.
 [20] U. Thumm, T. Niederhausen, and B. Feuerstein, *Phys. Rev. A* **77**, 063401 (2008).
 [21] V. Serov, A. Keller, O. Atabek, H. Figger, and D. Pavicic, *Phys. Rev. A* **72**, 033413 (2005).
 [22] W. A. Bryan *et al.*, *Phys. Rev. A* **76**, 023414 (2007).
 [23] F. Anis and B. D. Esry, *Phys. Rev. A* **77**, 033416 (2008).
 [24] T. Kunert and R. Schmidt, *Eur. Phys. J. D* **25**, 15 (2003).
 [25] See www.wavepacket.sourceforge.net
 [26] M. Magrakvelidze, F. He, T. Niederhausen, I. V. Litvinyuk, and U. Thumm, *Phys. Rev. A* **79**, 033410 (2009).